

This is the accepted manuscript made available via CHORUS. The article has been published as:

Smoothed dissipative particle dynamics model for mesoscopic multiphase flows in the presence of thermal fluctuations

Huan Lei, Nathan A. Baker, Lei Wu, Gregory K. Schenter, Christopher J. Mundy, and
Alexandre M. Tartakovsky

Phys. Rev. E **94**, 023304 — Published 5 August 2016

DOI: [10.1103/PhysRevE.94.023304](https://doi.org/10.1103/PhysRevE.94.023304)

Smoothed Dissipative Particle Dynamics model for mesoscopic multiphase flows in the presence of thermal fluctuations

Huan Lei¹, Nathan A. Baker¹, Lei Wu², Gregory K. Schenter¹,
Christopher J. Mundy¹, and Alexandre M. Tartakovsky¹

¹ *Pacific Northwest National Laboratory, Richland, WA 99354, USA,*

² *LMAM and School of Mathematical Sciences, Peking University, Beijing 100871 China*

Thermal fluctuations cause perturbations of fluid-fluid interfaces and highly nonlinear hydrodynamics in multiphase flows. In this work, we develop a novel multiphase smoothed dissipative particle dynamics model. This model accounts for both bulk hydrodynamics and interfacial fluctuations. Interfacial surface tension is modeled by imposing a pairwise force between SDPD particles. We show that the relationship between the model parameters and surface tension, previously derived under the assumption of zero thermal fluctuation, is accurate for fluid systems at low temperature but overestimates the surface tension for intermediate and large thermal fluctuations. To analyze the effect of thermal fluctuations on surface tension, we construct a coarse-grained Euler lattice model based on the mean field theory and derive a semi-analytical formula to directly relate the surface tension to model parameters for a wide range of temperatures and model resolutions. We demonstrate that the present method correctly models the dynamic processes, such as bubble coalescence and capillary spectra across the interface.

PACS numbers:

I. INTRODUCTION

Thermal fluctuations originating from molecular interactions can profoundly affect the behavior of multiphase fluid systems, resulting in emergent phenomena reflected on the hydrodynamic length scale. Consistent coupling of the molecular and hydrodynamic scales is at the heart of mesoscale framework development. At the fluid-fluid interface, capillary waves generated by thermal fluctuations result in stochastic and highly nonlinear interfacial dynamics [1]. This dynamics plays an important role in many physical and biological processes, such as spreading of nano droplets [2], breakup of nano-jets [3], Rayleigh-Taylor instabilities [4], and protein mobility within membranes [5]. Numerical modeling of such processes must accurately account for fluid momentum transport in bulk and interfacial dynamics under thermal fluctuations.

Traditionally, thermally driven mesoscale flows are described by so-called fluctuating hydrodynamics (FHD) (also known as Landau-Lifshitz-Navier-Stokes (LLNS)) equations [6]. These equations extend the hydrodynamic Navier-Stokes (NS) description by adding spatiotemporal delta-function-correlated random stress in the NS equations with the stress covariance determined from the fluctuation-dissipation theorem. Several numerical methods have been developed to solve LLNS equations, including finite difference [7–9], finite volume [10–14], and Lattice-Boltzmann methods [15]. Extending these grid-based methods to mesoscale multiphase and/or multicomponent flows requires coupling FHD with additional thermodynamic equations or appropriate boundary conditions at the interface between two fluids [16, 17]. Specifically, the interface between two fluids yields the FHD equations highly nonlinear, and it is nontrivial to numerically solve them with grid-based methods. Recently, grid-based methods have been used to solve coupled LLNS-free energy equations to model multiphase mesoscale flows (i.e., liquid and gas phases of the same fluid). For example, Shang *et al.* [17] solved the FHD equations coupled with the Ginzburg-Landau free energy model by using a heuristic correction for the observed unphysical negative density fluctuations across the interface. Donev *et al.* [18] solved the FHD equations coupled with a free energy model based on van der Waals equations. In this work, the surface tension is imposed through Korteweg stress, which requires further parameter calibration and can be sensitive to spatial discretization.

Lagrangian particle methods such as Smoothed Particle Hydrodynamics (SPH), Smoothed Dissipative Particle Dynamics (SDPD) and Dissipative Particle Dynamics (DPD) have been used for multiphase flow simulations as an alternative to the grid-based methods. Due to their Lagrangian nature, the particle methods are well suited for modeling multicomponent flow because they do not require any interface tracking schemes to evolve the interface between different fluid components. In these methods, each fluid is represented by its own set of particles with positions advected by fluid velocities. DPD is a meso-scale method, where each fluid particle represents a cluster of molecules. Forces acting between DPD particles are the combination of coarsened molecular forces and fluctuation forces related to each other through the fluctuation-dissipation theorem [19–22]. In SPH and SDPD, particles represent fluid volumes. Forces between SPH particles are obtained from the SPH discretization of the Navier-Stokes equations [23, 24]. SDPD was developed as a generalization of the SPH discretization of the Navier-Stokes equation [25] by

adding a fluctuation term to represent the effect of thermal fluctuations. The fluctuation term was constructed based on the so-called “general equation for non-equilibrium reversible-irreversible coupling” (GENERIC) framework [26, 27], which provides a systematic approach to construct the thermal fluctuation term in a thermodynamic consistent manner.

There are two main SPH approaches for imposing surface tension at fluid-fluid interfaces that can be extended to SDPD. The first approach is based on the Continuum Surface Force (CSF) method [28, 29] and requires estimating the local normal vectors and curvatures at the interface by means of a color function [29–31]. Accurate estimation of these variables requires sufficient resolution at the interface, i.e., the radii of the largest curvature corresponding to interfacial roughness should be much larger than the SPH smoothing parameter h , which plays the same role as grid size in grid-based methods. It has been demonstrated that the CSF-SDPD method yields accurate results for macroscopic multiphase flows where thermally induced interface oscillations are not pronounced [29]. For problems with large front oscillations, the effect of interfacial roughness on the CSF-SDPD accuracy requires additional investigations. The second approach is the PF-SPH method, where pairwise molecular-like forces are added into the SPH momentum conservation equation to produce surface tension at the fluid-fluid interface [32, 33]. Unlike the CSF-based SPH method, the PF-SPH method does not require estimates of the normal and curvature of the interface.

Particle methods have been extensively used for modeling complex fluids. For example, SDPD has been employed to simulate colloid suspensions [34, 35], polymer solution [36, 37], coupled molecular dynamics and continuum systems [38], and viscoelastic materials [39]. DPD has been used to model colloidal flows in porous media [40] and biofilm growth in shear flow [41]. A review of applications of DPD for modeling complex fluids and soft matter can be found in [42, 43]. A recent review of SPH applications to modeling multiphase flow, transport, and other environmental and engineered problems can be found in [44, 45].

In this paper, we present a rescaled Pairwise-Force Smoothed Dissipative Particle Dynamics (rPF-SDPD) method for mesoscale multicomponent flows. The rPF-SDPD model combines the Pairwise-Force Smoothed Particle Hydrodynamics (PF-SPH) method for multiphase multicomponent flows in the absence of thermal fluctuations [32, 33] with the Smoothed Dissipative Particle Dynamics (SDPD) method. In [46], the PF-SPH method was coupled with SDPD for a single-component quasi-two-phase (liquid-gas) system where the dynamics of gas phase was disregarded, i.e., only liquid phase was explicitly modeled. The major difference between PF-SPH and the present rPF-SDPD model is that rPF-SDPD accounts for the effect of interfacial thermal fluctuations on the interfacial surface tension and, therefore, can be used for predictive modeling of mesoscale multicomponent flows.

In the PF-SPH method, surface tension is imposed via molecular-like pairwise forces added into the SPH momentum conservation equation. The rPF-SDPD method can be derived from the PF-SPH by adding random forces, satisfying the fluctuation-dissipation theorem [26, 27]. A relationship between parameters in the pairwise force and the surface tension and temperature was not defined in [46]. In this work we fill this gap by proposing a scaling law for a two-component (two-fluid) system.

In this paper, we focus on moderate thermal fluctuations and their effects on the oscillations of the interface between fluids. Starting with the PF-SPH method, developed for low-temperature smooth interfaces (radii of curvature much greater than h), we analyze the effect of thermal-fluctuation-induced interface roughness by constructing a coarse-grained lattice model based on a mean field theory. The coarse-grained model enables us to extract a universal scaling relationship between surface tension and the thermal fluctuations for various model resolutions (i.e., h) and construct a semi-analytical relationship between the surface tension and model parameters. We demonstrate that the numerical values of the surface tension imposed by the proposed method agree well with the theoretical predictions based on the correct rescaled formulation. We also show that the structure factor of the perturbed interface correctly scales with the wave number.

In this work, we distinguish between macroscopic (in the absence of thermal fluctuations) and mesoscopic (in the presence of fluctuations) surface tensions and use the following notation:

- σ – mesoscopic surface tension across a nearly flat interface with local roughness induced by fluctuations due to the thermal energy $k_B T$
- σ_0 – macroscopic surface tension across flat and smooth interface (without local roughness)
- $\tilde{\sigma}(R, k_B T)$ – mesoscopic surface tension across the interface with curvature radii R and local roughness induced by fluctuations due to the thermal energy $k_B T$
- σ^N – numerical value of surface tension obtained from a direct simulation
- σ^F – surface tension obtained from numerical fitting to the scaling relationship.

The paper is organized as follows. Section II introduces the governing equations of the multiphase flow and their discrete SDPD counterparts. In Section III, we show that the “zero-thermal fluctuations” relationship between the

surface tension and force parameters overestimates the surface tension of mesoscale fluids in the presence of thermal fluctuations. To accurately account for the effect of thermal fluctuations, we introduce a coarse-grained lattice model based on the mean field theory. We establish a semi-analytical relationship between the temperature-dependent surface tension and model parameters through proper scaling among different model resolutions. In Section IV, we demonstrate that the present method yields consistent thermodynamic properties and further show that the present method captures the correct dynamic processes in multiphase flow, such as bubble coalescence dynamics and capillary wave spectra of an interface with and without external gravity field. Conclusions are given in Section V.

II. NUMERICAL MODEL

A. Governing equations

We consider the flow of α and β fluid components, occupying the domains $\Omega_\alpha(t)$ and $\Omega_\beta(t)$, respectively, with a sharp boundary $\Gamma(t) = \Omega_\alpha(t) \cap \Omega_\beta(t)$ separating the two fluids. We assume that at the mesoscale, flow of these fluids can be described by the isothermal stochastic Navier-Stokes equations [1], including the continuity equation

$$\frac{D\rho_l}{Dt} = -\rho_l (\nabla \cdot \mathbf{v}_l), \quad \mathbf{x} \in \Omega_l, \quad l = \alpha, \beta \quad (1)$$

and the momentum conservation equation

$$\frac{D\mathbf{v}_l}{Dt} = -\frac{1}{\rho_l} \nabla P_l + \frac{1}{\rho_l} \nabla \cdot \boldsymbol{\tau}_l + \mathbf{g} + \frac{1}{\rho_l} \nabla \cdot \mathbf{s}_l, \quad \mathbf{x} \in \Omega_l, \quad l = \alpha, \beta. \quad (2)$$

Here $D/Dt = \partial/\partial t + \mathbf{v}_l \cdot \nabla$ is the total derivative; ρ_l , \mathbf{v}_l , and P_l are the density, velocity, and pressure; and \mathbf{g} is the body force. The components of the viscous stress $\boldsymbol{\tau}_l$ are given by

$$\tau_l^{ik} = \mu_l \left(\frac{\partial v_l^i}{\partial x^k} + \frac{\partial v_l^k}{\partial x^i} \right), \quad (3)$$

where μ_l is the (shear) viscosity ($l = \alpha, \beta$) and the bulk viscosity of the l -fluid component is assumed to be equal to $\frac{2}{3}\mu_l$.

Fluctuations in velocity are caused by the random stress tensor

$$\mathbf{s}_l = \gamma_l \boldsymbol{\xi}, \quad (4)$$

where $\boldsymbol{\xi}$ is a random symmetric tensor (which components are random Gaussian variables), and γ_l is the strength of the noise. The random stress is related to the viscous stress by the fluctuation-dissipation theorem [47]. For incompressible and low-compressible fluids, the covariance of the stress components is:

$$\overline{s_l^{in}(\mathbf{x}_1, t_1) s_l^{jm}(\mathbf{x}_2, t_2)} = \gamma_l^2 \delta(\mathbf{x}_1 - \mathbf{x}_2) \delta(t_1 - t_2) \quad \gamma_l^2 = 2\mu_l k_B T \delta^{ij} \delta^{nm}, \quad (5)$$

where k_B is the Boltzmann constant, T denotes the temperature, $\delta(z)$ is the Dirac delta function, and δ^{ij} is the Kronecker delta function.

For generality, we treat the fluids as compressible and prescribe an equation of state $P_l = f(\rho_l)$ for each phase to close Eqs. (1) and (2). Eqs. (1) and (2) are subject to the no-slip boundary conditions for the fluid velocity at the fluid-solid boundary

$$v_{l,n} = 0 \quad \text{and} \quad v_{l,\tau} = 0, \quad l = \alpha, \beta, \quad (6)$$

and the dynamic Young-Laplace boundary condition for pressure and velocity at the fluid-fluid-interface

$$(P_\alpha - P_\beta) \mathbf{n} = (\boldsymbol{\tau}_\alpha - \boldsymbol{\tau}_\beta) \cdot \mathbf{n} + \kappa \sigma \mathbf{n}, \quad \mathbf{x} \in \Gamma, \quad (7)$$

where $v_{l,n}$ and $v_{l,\tau}$ are the normal and tangent components of velocity; κ is the curvature of the interface; and σ is the surface tension between α and β fluids. The normal vector \mathbf{n} is pointed away from the non-wetting phase. In this work, we are interested in the dynamics of fluid-fluid interfaces, so we will only consider cases not involving fluid-fluid-solid interfaces. Otherwise, the contact angle at the fluid-fluid-solid interface would also need to be prescribed. Eqs. (1) and (2) are subject to the initial conditions

$$\mathbf{v}_l(\mathbf{x}, t=0) = \mathbf{v}_l^0(\mathbf{x}), \quad \Omega_l(t=0) = \Omega_l^0, \quad \rho_l(\mathbf{x}, t) = \rho_l^0, \quad l = \alpha, \beta. \quad (8)$$

B. Smoothed Dissipative Particle Dynamics

In the SDPD method [25–27], the computational domains Ω_α and Ω_β are discretized with N_α and N_β points (usually referred to as particles) with initial positions \mathbf{r}_i^0 . It is convenient, but not necessary, to initially put particles on a Cartesian mesh with grid size Δ discretizing the domain $\Omega = \Omega_\alpha \cup \Omega_\beta$. The particles within domains Ω_α^0 and Ω_β^0 can then be labeled as α and β particles, respectively, and the particles are assigned the viscosities of the corresponding fluids. The mass of particle i in domain Ω_l is set to $m_i = \rho_l^0 \Delta^d$, and the particle number density is defined as $n_i = \rho_i/m_i$, where ρ_i is the density of the fluid carried by particle i . The initial particle number density of particle i is $n_i^0 = n_{eq} = \Delta^{-d}$, where d is the number of spatial dimensions. Eq. (2) is approximated as

$$\frac{D\mathbf{r}_i}{Dt} = \mathbf{v}_i, \quad m_i \frac{D\mathbf{v}_i}{Dt} = \sum_{j=1}^N (\mathbf{F}_{ij}^P + \mathbf{F}_{ij}^{visc} + \mathbf{F}_{ij}^S) + \mathbf{F}_i^b, \quad (9)$$

where $N = N_\alpha + N_\beta$ and the summation is over all particles,

$$\mathbf{F}_{ij}^P = - \left(\frac{P_j}{n_j^2} + \frac{P_i}{n_i^2} \right) \frac{\mathbf{r}_{ij}}{r_{ij}} \frac{dW(r_{ij}, h)}{dr_{ij}}, \quad (10)$$

$$\mathbf{F}_{ij}^{visc} = \frac{5(\mu_i + \mu_j)}{6n_i n_j} \frac{1}{r_{ij}} \frac{dW(r_{ij}, h)}{dr_{ij}} \left[\mathbf{v}_{ij} + \left(\mathbf{v}_{ij} \cdot \frac{\mathbf{r}_{ij}}{r_{ij}} \right) \frac{\mathbf{r}_{ij}}{r_{ij}} \right], \quad (11)$$

and \mathbf{F}_{ij}^S is

$$\mathbf{F}_{ij}^S = B_{ij} \frac{\mathbf{r}_{ij}}{r_{ij}} d\tilde{\mathcal{W}}_{ij}, \quad (12)$$

where $\mathbf{r}_{ij} = \mathbf{r}_i - \mathbf{r}_j$ and $r_{ij} = |\mathbf{r}_{ij}|$. In Eq. (12),

$$B_{ij} = \sqrt{-\frac{20}{6} k_B T \frac{(\mu_i + \mu_j)}{n_i n_j} \frac{1}{r_{ij}} \frac{dW(r_{ij}, h)}{dr_{ij}}}, \quad (13)$$

$d\tilde{\mathcal{W}}_{ij} = (d\mathcal{W}_{ij} + \mathcal{W}_{ij}^T)$, and \mathcal{W}_{ij} is the matrix of independent increments of the Wiener process.

The random number $\tilde{\zeta}_{ji}^l = \tilde{\zeta}_{ji}^l$ has a Gaussian distribution with zero mean and unit variance, and superscript l denotes l -component of vectors. \mathbf{F}_i^b is the body (e.g., gravitational) force acting on particle i . In the preceding expressions, W is the "smoothed" Dirac delta function with compact support h , which integrates to one, and in the limit of $h \rightarrow 0$ approaches the Dirac delta function. In this work, we use W in the form of the fourth-order spline function [48]:

$$W(r, h) = \frac{81}{359\pi h^3} \begin{cases} \left(3 - \frac{3|r|}{h}\right)^5 - 6\left(2 - \frac{3|r|}{h}\right)^5 + 15\left(1 - \frac{3|r|}{h}\right)^5 & 0 \leq |r| < \frac{1}{3} h \\ \left(3 - \frac{3|r|}{h}\right)^5 - 6\left(2 - \frac{3|r|}{h}\right)^5 & \frac{1}{3}h \leq |r| < \frac{2}{3} h \\ \left(3 - \frac{3|r|}{h}\right)^5 & \frac{2}{3}h \leq |r| < h \\ 0 & |r| > h \end{cases} \quad (14)$$

In Eq. (9), $\sum_{j=1}^N F_{ij}^P$ and $\sum_{j=1}^N \mathbf{F}_{ij}^{visc}$ terms are obtained using the SPH discretization of the ∇P and $\mu \nabla^2 \mathbf{v}$ terms in the NS equation, respectively. The \mathbf{F}_{ij}^S force is derived from the expression (11) of the viscous/dissipative force using the fluctuation-dissipation theorem instead of directly discretizing the $\nabla \cdot \mathbf{s}$ term in Eq. (2). The number density n_i can be computed by integrating an ordinary differential equation (ODE) obtained from the SPH discretization of the continuity equation (1), but it is more common in SDPD to compute density as

$$n_i = \sum_j W(r_{ij}, h). \quad (15)$$

In this work, we use the equation of state

$$P = \frac{c^2 \rho_0}{7} \left[\left(\frac{\rho}{\rho_0} \right)^7 - 1 \right], \quad (16)$$

where c is the speed of sound and ρ_0 is the equilibrium density.

C. Pairwise-Force Smoothed Dissipative Particle Dynamics for low-temperature multicomponent flows

To impose the boundary condition (7), we add the pairwise interaction forces

$$\mathbf{F}_{ij}^{int} = \mathbf{F}^{int}(\mathbf{r}_{ij}) = -s_{ij}\phi(r_{ij})\frac{\mathbf{r}_{ij}}{r_{ij}} \quad (17)$$

into the momentum equation,

$$m_i \frac{D\mathbf{v}_i}{Dt} = \sum_{j=1}^N (\mathbf{F}_{ij}^P + \mathbf{F}_{ij}^{visc} + \mathbf{F}_{ij}^S + \mathbf{F}_{ij}^{int}) + \mathbf{F}_i^b, \quad (18)$$

where $\phi(r_{ij})$ is the so-called shape factor, to be defined later, and

$$s_{ij} = \begin{cases} s_{\alpha\beta}, & \mathbf{r}_i \in \Omega_\alpha \text{ and } \mathbf{r}_j \in \Omega_\beta, \\ s_{\alpha\alpha}, & \mathbf{r}_i \in \Omega_\alpha \text{ and } \mathbf{r}_j \in \Omega_\alpha, \\ s_{\beta\beta}, & \mathbf{r}_i \in \Omega_\beta \text{ and } \mathbf{r}_j \in \Omega_\beta. \end{cases} \quad (19)$$

The force \mathbf{F}_{ij}^{int} is a molecular-like pairwise interaction force acting between particle i of the α phase and particle j of the β phase. The shape function ϕ is selected such that \mathbf{F}_{ij}^{int} behaves as a pairwise molecular force, i.e., \mathbf{F}_{ij}^{int} is short-range repulsive ($F_{\alpha,\beta}(r_{ij} \leq r^*) < 0$, $r^* < h$) and long-range attractive ($F_{\alpha,\beta}(r^* < r_{ij} \leq h) > 0$). For computational efficiency, ϕ should be zero (or decay rapidly) for $r_{ij} \geq h$. A similar approach to impose the boundary conditions (7) has been used in an SPH multiphase flow model [33, 49, 50] and in SPH and SDPD models for a single-phase flow with a free surface [32, 46, 51, 52].

Various forms of ϕ have been proposed in literature, and it has been shown that ϕ affects particle distribution. Here, in three-dimensional simulations we use

$$\phi = r_{ij} \left[-Ae^{-\frac{r_{ij}^2}{2r_a^2}} + e^{-\frac{r_{ij}^2}{2r_b^2}} \right], \quad (20)$$

where $A=8$, $r_a = r_b/2 = \Delta/2 = n_{eq}^{-1/3}/2$, which we found to result in a relatively uniform particle distribution for a given surface tension value.

It has been demonstrated that, in the absence of thermal fluctuations (i.e., for $\mathbf{F}_{ij}^S = 0$), the parameters in \mathbf{F}_{ij}^{int} can be related to the “macroscopic” surface tension σ_0 as

$$s_{\alpha\alpha} = s_{\beta\beta} = 10^3 s_{\alpha\beta} = \frac{1}{2(1-10^{-3})} n_{eq}^{-2} \frac{\sigma_0}{\lambda}, \quad (21)$$

and

$$\lambda = \frac{\pi}{8} \int_0^\infty z^4 \phi(z) dz = \pi(-Ar_a^6 + r_b^6). \quad (22)$$

The expression (21) is obtained using the Gibbs treatment [53], where σ is related to the total fluid stress as

$$\sigma(\mathbf{x}) = \int_{-\infty}^{+\infty} [T_\tau(z) - T_n(z)] dz, \quad \mathbf{x} \in \Gamma. \quad (23)$$

Here, $T_n(z) = T_{zz}(z)$ and $T_\tau(z)$ are the normal and tangent components of the stress, and the integration is done along the line crossing Γ in the normal direction at point \mathbf{x} .

The stress \mathbf{T} can be found in terms of the forces acting between SDPD particles according to the Hardy formula [54]:

$$\mathbf{T}(\mathbf{x}) = \mathbf{T}_{(c)}(\mathbf{x}) + \mathbf{T}_{(int)}(\mathbf{x}), \quad (24)$$

where $\mathbf{T}_{(c)}(\mathbf{x})$ is the convection stress,

$$\mathbf{T}_{(c)}(\mathbf{x}) = - \sum_{j=1}^N m_j (\bar{\mathbf{v}}(\mathbf{x}) - \mathbf{v}_j) \otimes (\bar{\mathbf{v}}(\mathbf{x}) - \mathbf{v}_j) \tilde{\psi}_\eta(\mathbf{x} - \mathbf{r}_j), \quad (25)$$

and $\mathbf{T}_{(int)}(\mathbf{x})$ is the interaction stress,

$$\mathbf{T}_{(int)}(\mathbf{x}) = \frac{1}{2} \sum_{i=1}^N \sum_{j=1}^N \mathbf{f}_{ij} \otimes (\mathbf{r}_j - \mathbf{r}_i) \int_0^1 \tilde{\psi}_\eta(\mathbf{x} - s\mathbf{r}_i - (1-s)\mathbf{r}_j) ds, \quad (26)$$

where $\bar{\mathbf{v}}(\mathbf{x}) = \sum_j m_j \mathbf{v}_j \tilde{\psi}_\eta(\mathbf{x} - \mathbf{r}_j) \left(\sum_j m_j \tilde{\psi}_\eta(\mathbf{x} - \mathbf{r}_j) \right)^{-1}$ is the average velocity and $\mathbf{f}_{ij} = \mathbf{F}_{ij}^P + \mathbf{F}_{ij}^{visc} + \mathbf{F}_{ij}^S + \mathbf{F}_{ij}^{int}$ is the total force acting between a pair of i and j particles. The summation here is over all particles, and \otimes denotes a dyadic product of vectors. The weighting function $\tilde{\psi}(\mathbf{x})$ is a “smooth” approximation of the Dirac delta function and can be chosen fairly arbitrary. Here, we assume that $\tilde{\psi}(\mathbf{x})$ is the product of one-dimensional functions $\psi_{\eta,l} = \frac{1}{\eta} \psi(\mathbf{x}_{(l)})$, where $l = 1, 2, 3$ denotes a vector component. The function $\psi_{\eta,l}(\mathbf{x})$ has compact support η , or becomes sufficiently small for $|\mathbf{r}| > \eta$. In our calculations, we set $\eta = h$.

The surface tension between any two fluids only depends on the properties of the two fluids and (weakly depends) on the radii of the interface curvature, but not on the fluid velocities. As shown in Sec. IV B, the modeled surface tension in our model is independent of curvature smaller than $\frac{1}{2h}$ for a wide range of temperatures. To derive the relationship between \mathbf{F}_{ij}^{int} and σ , we first assume the two fluids are separated by an interface with the radii of curvature much larger than η (and h). The dependence of surface tension on large curvatures will be addressed in Section IV B. Under the assumption of small curvature, the interface can be locally treated as flat. Because the surface tension is independent of flow conditions, without loss of generality, we consider the system at equilibrium. It should be noted that in the presence of thermal fluctuations, SDPD particles move, even at equilibrium. However, in the following derivations, we disregard the mesoscale effects and compute the macroscale surface tension σ_0 , i.e., we assume that $\mathbf{F}_{ij}^{visc} + \mathbf{F}_{ij}^S$ and $\mathbf{T}_{(c)}$ have zero net contribution to σ_0 . Furthermore, it was demonstrated in [33] that if the same average particle density is used to discretize both fluid phases, then the \mathbf{F}_{ij}^P has exactly zero contribution to the surface tension. Finally, Eq. (23) can be replaced with

$$\sigma_0(\mathbf{x}) = \int_{-\infty}^{+\infty} [\tilde{T}_\tau(z) - \tilde{T}_n(z)] dz, \quad \mathbf{x} \in \Gamma \quad (27)$$

where $\tilde{T}_n(z) = \tilde{T}_{zz}(z)$ and $\tilde{T}_\tau(z)$ are the normal and tangent components of the stress

$$\tilde{\mathbf{T}}_{(int)}(\mathbf{x}) = \frac{1}{2} \sum_{i=1}^N \sum_{j=1}^N \mathbf{F}_{ij}^{int} \otimes (\mathbf{r}_j - \mathbf{r}_i) \int_0^1 \tilde{\psi}_\eta(\mathbf{x} - s\mathbf{r}_i - (1-s)\mathbf{r}_j) ds. \quad (28)$$

The next step in deriving Eq. (21) and (22) is to approximate Eq. (28) with

$$\tilde{\mathbf{T}}_{(int)}(\mathbf{x}) = -\frac{1}{2} n_{eq}^2 \int_{\Omega} \int_{\Omega} g(\mathbf{r}', \mathbf{r}'') \mathbf{F}^{int}(\mathbf{r}' - \mathbf{r}'') \otimes (\mathbf{r}' - \mathbf{r}'') \int_0^1 \tilde{\psi}_\eta(\mathbf{x} - s\mathbf{r}' - (1-s)\mathbf{r}'') ds d\mathbf{r}' d\mathbf{r}'', \quad (29)$$

where $g(\mathbf{r}', \mathbf{r}'')$ is the pair distribution function [55]. Assuming that

$$g(\mathbf{r}', \mathbf{r}'') = \begin{cases} g_{\alpha\beta}(|\mathbf{r}' - \mathbf{r}''|), & \mathbf{r}' \in \Omega_\alpha \text{ and } \mathbf{r}'' \in \Omega_\beta, \\ g_{\alpha\alpha}(|\mathbf{r}' - \mathbf{r}''|), & \mathbf{r}' \in \Omega_\alpha \text{ and } \mathbf{r}'' \in \Omega_\alpha, \\ g_{\beta\beta}(|\mathbf{r}' - \mathbf{r}''|), & \mathbf{r}' \in \Omega_\beta \text{ and } \mathbf{r}'' \in \Omega_\beta, \end{cases} \quad (30)$$

substituting Eq. (29) in Eq. (27) and integrating the latter yields

$$\sigma_0 = s_{\alpha\alpha} \frac{\pi}{8} n_{eq}^2 \int_0^\infty g_{\alpha\alpha}(r) \phi(r) r^4 dr + s_{\beta\beta} \frac{\pi}{8} n_{eq}^2 \int_0^\infty g_{\beta\beta}(r) \phi(r) r^4 dr - 2s_{\alpha\beta} \frac{\pi}{8} n_{eq}^2 \int_0^\infty g_{\alpha\beta}(r) \phi(r) r^4 dr. \quad (31)$$

Eq. (31) is an extension of an expression for the surface tension of a single-component multiphase molecular system (an α -liquid in equilibrium with its gas phase) given in [53]. This expression assumes that molecules are interacting via a pairwise force $s_{\alpha\alpha} \tilde{\phi}(r)$, $s_{\beta\beta} = s_{\alpha\beta} = 0$, and n_{eq} is the particle density of the liquid phase. To make expression

(31) computable, $g_{kl}(r)$ ($(k, l) = \alpha, \beta$) must be defined. A simple approximation is $g(r) = 1$, which is equivalent to treating Eq. (28) as a Riemann sum. This reduces Eq. (29) to an expression obtained by Rayleigh [56] for a surface tension between two fluids made of molecules interacting via the pairwise force $s_{kl}\tilde{\phi}(r)$ ($(k, l) = \alpha, \beta$). Under the assumption $g(r) = 1$, Eqs. (21) and (22) follow directly from Eq. (31). The details of integration in Eq. (31) in two spatial dimensions are given in [33], and the extension to the three-dimensional case is straightforward.

Remark II.1 *We emphasize that Eqs. (21) and (31) are derived with the assumption that the interface between Ω_α and Ω_β is flat, and that these equations should hold for any interface with the radii of the largest curvature much larger than h , the range of the SDPD forces. In the next section, we show that Eqs. (21) and (31) accurately describe the relationship between the surface tension and pairwise forces for macroscopic systems (where thermal fluctuations are relatively small or absent) characterized by σ_0 . For a mesoscale fluid system, the interfacial roughness, induced by thermal fluctuations, may affect the surface tension σ . In the following section, we quantify the relationship between σ , σ_0 , $k_B T$, and other model parameters.*

III. EFFECT OF THERMAL FLUCTUATIONS: MEAN FIELD THEORY ANALYSIS AND NUMERICAL ERROR QUANTIFICATION

In this section, we study temperature dependence of the surface tension for the model introduced in Section II. First, we validate the method by comparing the surface tension from direct simulation with the value prescribed by Eq. (21). Here, we prescribe “low” temperatures (to be rigorously defined in Section III D) to keep thermally induced fluctuations small and the fluid interface essentially flat. In this context, the low temperature refers to the macroscopic limit of the SDPD model, where thermal fluctuations are negligible, rather than the absolute low state of thermal energy.

Next, we demonstrate that, for higher temperatures, Eq. (21) overestimates the surface tension by a value further dependent on n_{eq} .

To explore the effect of thermal fluctuations on the surface tension, we construct an Euler lattice model based on mean field theory and obtain a universal scaling relationship that accounts for the effect of interfacial roughness for various thermal fluctuations and model resolutions. We then propose a semi-analytical formula to relate the surface tension to model parameters and quantify the numerical error for different temperatures and model resolutions.

A. Low temperature

We numerically compute the surface tension between two fluids separated by a nearly flat interface using Eq. (23). We model a layer of one fluid surrounded by two layers of another fluid with $n_{eq} = 27, 46.656, 64$, and 91.125 . In all of these simulations, the temperature, speed of sound, and surface tension are set to $k_B T = 0.001$, $c = 6.0$, and $\sigma_0 = 2.1$, respectively. The parameters $s_{\alpha\alpha}$, $s_{\beta\beta}$, and $s_{\alpha\beta}$ are found from Eq. (21). The temperature is chosen so the fluid interface remains essentially flat. The simulation domain size is $10 \times 10 \times 16$ with fluid α placed between $-3 < z < 3$ and fluid β occupying the rest of the domain. The periodic boundary conditions are used in all directions.

Figure 1(a) shows an example of the normal and tangent stresses across the interface for $n_{eq} = 27$. Similar computations are conducted for other number densities. For each combination of parameters, 10 independent simulations are performed, and T_τ and T_n are computed using the simulation data from the last 10000 time steps. Figure 1(b) shows the relative numerical error, $\varepsilon = |1 - \sigma^N/\sigma_0|$, for different n_{eq} . Here, σ^N is the surface tension obtained from direct simulations using Eq. (23). As n_{eq} increases from 27 to 64, ε decreases from 4.7% to 2.4%, respectively. However, ε does not further decrease as n_{eq} increases from 64 to 91.125. One possible reason for this plateau result is the uniform distribution assumption, $g(r) \equiv 1$, in the derivation of Eq. (21), which is not fully satisfied even for large n_{eq} . Nevertheless, for all considered n_{eq} , the error is less than 5%.

B. Effect of thermal fluctuations

In this section, we model the multiphase system, described in Section III A, with different temperatures. Figure 2 shows the computed surface tension for different n_{eq} , with $k_B T$ between 0 and 0.06. As $k_B T$ increases, the interfacial roughness gets more pronounced (also see Sec. IV D), and the surface tension decreases accordingly. Eq. (21) accurately predicts the surface tension at the low temperature, but it overestimates the surface tension at higher temperatures. Moreover, we observe that the simulated surface tension values, obtained at different $k_B T$, further

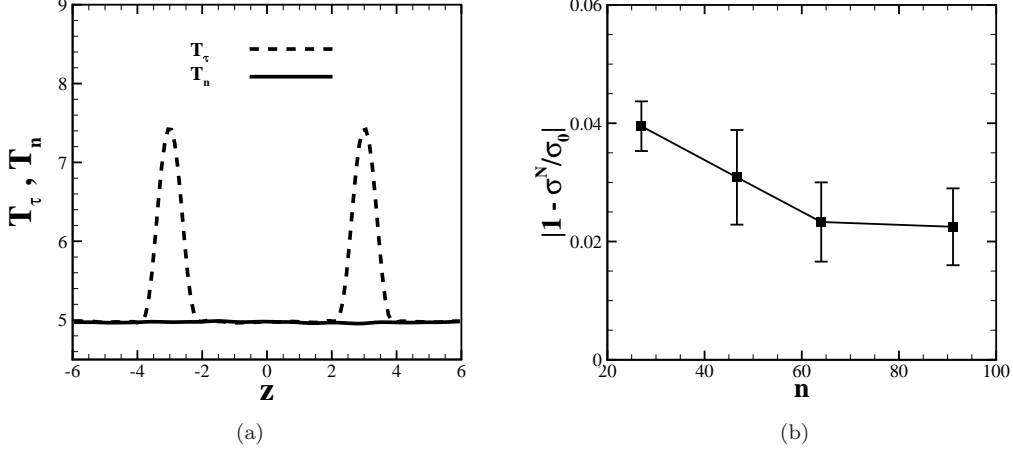


FIG. 1: (a) Normal and tangential hardy stress T_n and T_τ computed across the interface of the two-phase fluid layer located at $z = -3.0$ and $z = 3.0$. (b) Numerical error of imposed surface tension versus n_{eq} at $k_B T = 0.001$.

depend on n_{eq} . Given the same value at the low-temperature limit, the surface tension exhibits different temperature-dependent behaviors for different n_{eq} . For low resolutions (e.g., $n_{eq} = 27$), the surface tension shows weak dependence on T , while for high resolutions, the surface tension decreases more rapidly as T increases. To model multiphase flow with thermal fluctuations, we need to understand the relationship between σ and σ_0 , $k_B T$, and n_{eq} .

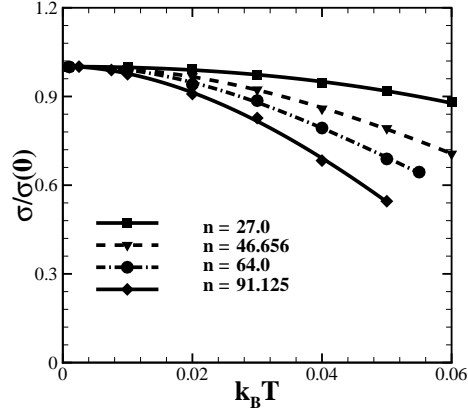


FIG. 2: Surface tension between the two-phase flow computed at different temperatures.

C. Coarse-grained lattice model

To quantify the effect of thermal fluctuation on the surface tension, we coarse grain the system by replacing the present Lagrangian particle system with a Euler lattice, similar to the work of [53, 57, 58]. Figure 3 shows a sketch of the mapping process. For each model resolution with $n_{eq} = \Delta^{-3}$ (in three spacial dimensions), we map the system on the lattice with the lattice size Δ . For each lattice unit, we define the number density of each lattice (i, j, k) as n_{ijk}^L . Given a flat interface, $n^L = 1$ within the α fluid region and 0, otherwise.

For each lattice unit, we assume the energy can be approximated by a mean field, i.e., $u^L = \epsilon n^L$, where ϵ is the potential energy of the lattice filled with an SDPD particle

$$\epsilon = \int_0^\infty 4\pi u(r)g(r)r^2 dr \approx \int_0^\infty 4\pi u(r)r^2 dr, \quad (32)$$

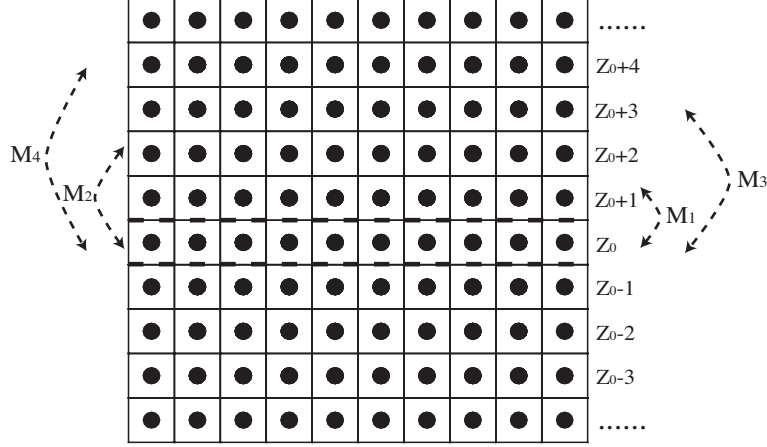


FIG. 3: A sketch of the coarse-grained lattice model, where the Lagrangian-based particle model is mapped into a discrete lattice. The lattice layer z_0 (e.g., the one between the horizontal dashed lines) interacts with the neighboring layers $z_0 \pm 1$, $z_0 \pm 2$, \dots , $z_0 \pm L$ with interaction energy M_1 , M_2 , \dots , M_L , respectively.

where $u(r)$ is the potential energy between two fluid particles due to the interaction force, $du(r)/dr = s_{\alpha\alpha}\phi(r)$. Similar to Ref. [53], we define the activity $\zeta(n^L, k_B T)$ for each lattice unit, such that the probability to fill the lattice with an SDPD particle is

$$n^L/\zeta = (1 - n^L)e^{-u^L/k_B T}. \quad (33)$$

Therefore, the activity of each lattice unit is given by

$$\zeta(n^L, k_B T) = \frac{n^L}{1 - n^L} e^{\epsilon n^L/k_B T}. \quad (34)$$

Under equilibrium conditions, the equilibrium activity ζ satisfies the equal area rule [53]

$$\int_{n_g^L}^{n_l^L} \ln \left[\frac{\zeta(n', k_B T)}{\zeta} \right] dn' = 0, \quad \zeta(n_g^L) = \zeta(n_l^L) \quad (35)$$

where n_g^L and n_l^L are the nontrivial solutions ($\neq 0.5$) corresponding to the coexisting densities of the gas and liquid phases. This gives the equilibrium activity ζ by

$$\zeta = e^{\epsilon/2k_B T}. \quad (36)$$

Next, we consider the inhomogeneous fluid system. Without loss of generality, we assume the interface is normal to z direction and denote the lattice number density as $n^L(z)$. As shown in Figure 3, the lattice unit at layer z_0 interacts with the neighboring layers $z_0 - L, z_0 - L + 1, \dots, z_0, \dots, z_0 + L - 1, z_0 + L$, where L is determined by the cut-off distance of pairwise force interaction h and lattice unit length Δ by

$$L = \left\lceil \frac{h}{\Delta} \right\rceil. \quad (37)$$

The energy $u^L(z_0)$ of a lattice unit at layer z_0 is determined by the interaction energy with the neighboring layers, which is given by

$$\begin{aligned} u^L(z_0) &= \epsilon n^L(z_0) + \sum_{l=1}^L M_l \Delta_l^2 n^L(z_0) \\ \Delta_l^2 n^L(z_0) &= n^L(z_0 + l) + n^L(z_0 - l) - 2n^L(z_0), \end{aligned} \quad (38)$$

where $\epsilon n^L(z_0)$ represents the energy of the lattice unit under homogeneous assumption, M_l represents the interaction energy between two layers of homogeneous fluid with distance $l\Delta$, and $M_l(n^L(z_0 + l) - n^L(z_0))$ represents the change of potential energy if the number density of the $(z_0 + l)th$ layer is changed from homogeneous assumption to $n^L(z_0 + l)$.

M_l is related to the forces acting between SDPD particles, including \mathbf{F}_{ij}^{int} , and can be determined in an iterative manner. As shown in Figure 3, we first consider the interaction between layer z_0 and $z_0 + L$. For a single particle in layer $z_0 + L$ with distance z to the upper layer z_0 , the attractive force is

$$\psi(z) = \int_z^\infty 2\pi z' n_{eq} u(z) dz'. \quad (39)$$

Therefore, the total interaction force between layers z_0 and $z_0 + l$ is

$$\theta(z) = \int_{(L-1)\Delta}^\infty \psi(z') n_{eq} dz', \quad (40)$$

and the interaction energy M_L between layers z_0 and $z_0 + L$ is

$$W_L = \int_{(L-1)\Delta}^\infty \theta(z') dz', \quad M_L = W_L. \quad (41)$$

Next, we consider the interaction energy W_{L-1} between the layers $[z_0 - 1, z_0]$ and $[z_0 + L - 1, z_0 + L]$. We note that the interaction energy between layer z_0 and $z_0 + L$, as well as layer $z_0 - 1$ and $z_0 + L - 1$, is M_L . Analysis, similar to Eqs. (40) and (41), gives

$$W_{L-1} = \int_{(L-2)\Delta}^\infty \theta(z') dz', \quad 2M_L + M_{L-1} = W_{L-1}. \quad (42)$$

Repeating the preceding process, M_l can be obtained as

$$\begin{aligned} \sum_{k=l}^L (k - l + 1) M_k &= W_l \\ W_l &= \int_{(l-1)\Delta}^\infty \theta(z') dz', \end{aligned} \quad (43)$$

where M_{l+1}, \dots, M_L are found iteratively.

Combining Eqs. (32), (36), and (43), we can rewrite Eq. (33) as [57]

$$\begin{aligned} - \sum_{l=1}^L M_l \Delta_l^2 n^L(z) &= F' [n^L(z)], \\ F' [n^L(z)] &= -\epsilon \left(\frac{1}{2} - n^L(z) \right) + k_B T \ln [n^L / (1 - n^L)]. \end{aligned} \quad (44)$$

This is the governing equation for the inhomogeneous density $n^L(z)$ of the coarse-grained lattice model, with asymptotic solutions $n^L(-\infty) = n_g^L$ and $n^L(\infty) = n_l^L$ satisfying

$$F'(n_g^L) = F'(n_l^L) = 0. \quad (45)$$

By solving Eq. (44), we can explore the intrinsic relationship between the Lagrangian particle model and the coarse-grained lattice model, as well as quantify the effect of the thermal fluctuations of the surface tension for different n_{eq} , as discussed in Section III D.

D. Effect of thermal fluctuations: scaling and error analysis

The numerical solution of Eq. (44) is complicated by a stiff nonlinear term $k_B T \ln [n^L/(1 - n^L)]$. To simplify the problem, we introduce the change of variables

$$n^L(z) = \frac{e^{x(z)}}{1 + e^{x(z)}}, \quad (46)$$

rewrite Eq. (44) as

$$\begin{aligned} -\sum_{l=1}^L M_l \delta_l^2 x(z) &= -\epsilon \left(\frac{1}{2} - \frac{e^{x(z)}}{1 + e^{x(z)}} \right) + k_B T x(z), \\ \delta_l^2 x(z) &= \frac{e^{x(z+l)}}{1 + e^{x(z+l)}} + \frac{e^{x(z-l)}}{1 + e^{x(z-l)}} - \frac{2e^{x(z)}}{1 + e^{x(z)}}, \end{aligned} \quad (47)$$

and solve it using the Newton-Raphson method on the discrete lattice plane at $z = \dots, -3/2, -1/2, 1/2, 3/2, \dots$. The surface tension of the lattice model can be determined as

$$\begin{aligned} \sigma &= \sum_{z=-\infty}^{\infty} \left\{ F[n^L(z)] + \frac{1}{2} \sum_{l=1}^L M_l [\Delta_l n^L(z)]^2 \right\} \\ \Delta_l n^L(z) &= n^L(z+l) - n^L(z), \quad F(n) = \int_{n_g}^{n_l} F'(n) dn. \end{aligned} \quad (48)$$

To explore the effect of thermal fluctuations on the modeled surface tension, we map the Lagrangian SDPD particles with different n_{eq} on a discrete lattice following the procedure introduced in Section III C. For each n_{eq} , we choose $\sigma = 2.1$ at $k_B T = 0.001$ similar to Section III A and solve Eq. (44) numerically with ϵ and M_l obtained from Eqs. (32) and (43), respectively.

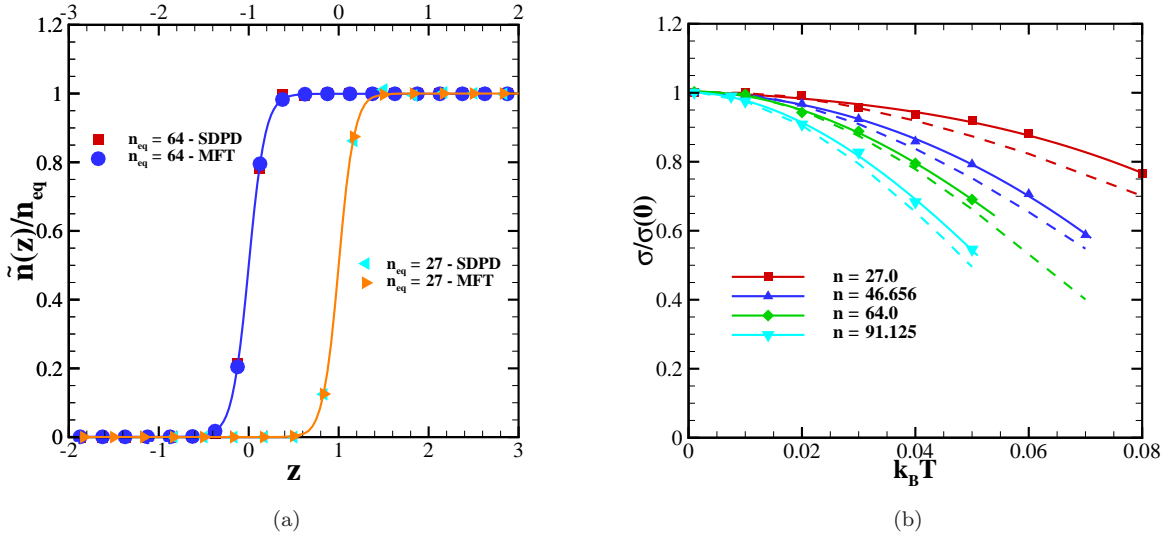


FIG. 4: (a) Normalized interfacial density profile $\tilde{n}(z)$ obtained from both the direct SDPD simulation and the mean field theory from Eq. (44) at $k_B T = 0.03$. For the SDPD model, $\tilde{n}(z)$ is defined as the number density of the SDPD particle with the binning size as Δ along the z direction. (b) Temperature-dependent surface tension obtained from the direct simulation and the present lattice model. $\sigma(0)$ represents the numerical value of the surface tension at $k_B T = 0.001$.

Figure 4(a) compares the density profiles obtained from the the direct simulations and the lattice model with $n_{eq} = 27$ and 64 and $k_B T = 0.03$. In the lattice model, we numerically solve Eq. (47) with ϵ and M_l , obtained from Eqs. (32) and (43), respectively. Good agreement is achieved for both $n_{eq} = 27$ and $n_{eq} = 64$. Figure 4(b) shows the surface tensions obtained from the SDPD lattice models for different $k_B T$ values. It can be seen that the lattice model

successfully captures the modeled surface tension's dependence on $k_B T$ and n_{eq} . The difference in σ obtained from the lattice model and SDPD is mainly due to the mean field approximation of the energy in Eqs. (32) and (38). As n_{eq} increases, the agreement between the two models improves. This result not only validates the intrinsic relationship between the present method and the coarse-grained lattice model, established through Eqs. (32), (43), and (38), but also indicates that the lattice model is a convenient tool for studying the effect of thermal fluctuations on the surface tension in the present model.

Inspired by the lattice model, we revisit Eq. (35). It is possible to define the transition temperature

$$-\epsilon^L / (k_B T_c)^L = 4, \quad (49)$$

above which only the trivial solution exists. Here, the superscript “ L ” represents the unit lattice length scale Δ . With $k_B T = k_B T_c^L$, Eq. (35) only has the trivial solution $n_g^L = n_l^L = 0.5$, and the surface tension decays to 0.

We compute ϵ from Eq. (32) for different n_{eq} and represent the results in the lattice model units. Because ϵ and $k_B T$ scale with length unit $[L]$ as $\epsilon \sim [L]^5$ and $k_B T \sim [L]^2$, where $[L]$ represents the length unit of the lattice model, we have

$$-\frac{\epsilon / (\Delta)^5}{k_B T_c / (\Delta)^2} = 4. \quad (50)$$

For $n_{eq} = 27, 46.656, 64$, and 91.125 , the predicted transition temperature $k_B T_c$ is 0.198, 0.135, 0.108, and 0.087, respectively.

These results indicate that although the particle model of different spatial resolution yields the same surface tension when $k_B T$ approaches zero, the transition temperature of the corresponding lattice model is different, leading to different temperature-dependent surface tensions for large $k_B T$. Another way to understand this is to note that the SDPD fluid of different n_{eq} modeled by Eq. (21) yields the same interaction energy (i.e., $\sum_{l=1}^L l M_l$) and, therefore, the same surface tension between neighboring layers. However, the total energy ϵ^L varies for different n_{eq} , leading to a dependence of σ on n_{eq} . In particular, smaller n_{eq} yields larger ϵ^L , leading to a smaller response to interfacial fluctuations. Therefore, σ decays more slowly for low n_{eq} when $k_B T$ increases.

Based on the preceding analysis, we propose a scaling relationship that relates the surface tension to the model parameters for different n_{eq} , i.e.,

$$\sigma(k_B T, n_{eq}, \epsilon) = f\left(\frac{k_B T}{n_{eq} \epsilon}\right), \quad (51)$$

where ϵ is determined by Eq. (32) and the functional form of f depends on the form of \mathbf{F}_{ij}^{int} .

Eq. (51) is the main theoretical result of this study. It suggests that the imposed surface tension at $k_B T$, $\sigma(k_B T)$ can be related to the parameters of the rPF-SDPD model, including $k_B T$, n_{eq} , and surface tension at the “macroscopic” interface with zero thermal fluctuations, σ_0 , through a unified scaling relationship. For the \mathbf{F}_{ij}^{int} given by Eq. (20) and used in this study, we propose an approximate form for f

$$\sigma^F(k_B T, n_{eq}, \epsilon) = \sigma_0 \left(1 - b \left(\frac{k_B T}{n_{eq} \epsilon}\right)^2\right)^2, \quad (52)$$

where $b = 12.4$ is a fitting parameter.

Figure 5 shows the surface tension values σ obtained from the rPF-SDPD model and the scaling formula Eq. (52) as a function of $\frac{k_B T \Delta^3}{\epsilon}$. The simulation results agree well with the scaling formula for all considered n_{eq} , with agreement improving with increasing n_{eq} .

Table I shows the relative differences $\varepsilon = |1 - \sigma^N(k_B T) / \sigma^F(k_B T)|$, where σ^N and σ^F are the surface tension values obtained from direct simulation of rPF-SDPD and fitting to scaling relationship Eq. (51) through Eq. (52), respectively. For all cases, ε is less than 5.7% and decreases with increasing n_{eq} . This shows that Eq. (52) accurately describes the relationship between the surface tension and \mathbf{F}_{ij}^{int} , n_{eq} , and $k_B T$. In the next section, we demonstrate the accuracy and capabilities of rPF-SDPD by applying it to several mesoscale multicomponent systems.

E. Parameterization of the rPF-SDPD model

In this study, all simulations are carried out in the model units, which are related to the physical units in a standard manner. In addition, there are several model parameters related to the rPF-SDPD discretization that need to be

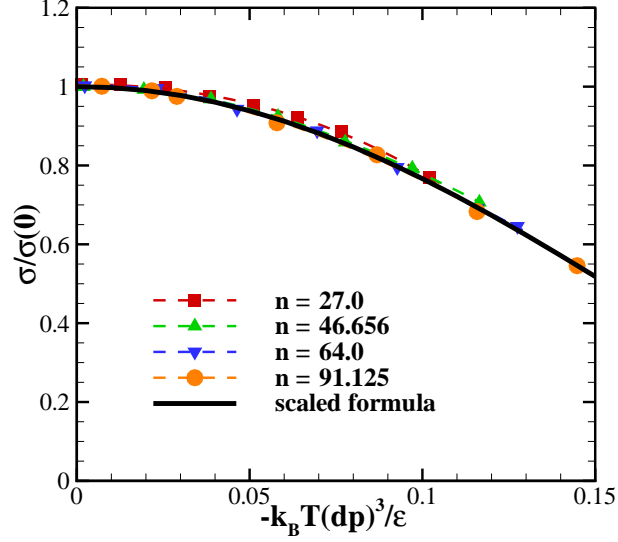


FIG. 5: Surface tension with respect to $-\frac{k_B T \Delta^3}{\epsilon}$ obtained from the direct simulation and Eq. (52). $\sigma(0)$ represents the numerical value of the surface tension at $k_B T = 0.001$.

n	$k_B T = 0.001$	$k_B T = 0.01$	$k_B T = 0.02$	$k_B T = 0.03$	$k_B T = 0.04$	$k_B T = 0.05$	$\langle \varepsilon \rangle$
27.0	3.80%	4.23%	4.71%	4.57%	4.96%	5.64%	4.88%
46.656	3.02%	3.19%	3.57%	3.68%	3.40%	4.67%	3.61%
64.0	2.15%	2.75%	1.45%	2.44%	1.63%	1.47%	2.17%
91.125	2.09%	1.98%	1.47%	0.80%	2.59%	3.17%	1.49%

TABLE I: Relative error $\varepsilon = |1 - \sigma^N(k_B T)/\sigma^F(k_B T)|$ between the direct simulated surface tension $\sigma^N(k_B T)$ and the prediction $\sigma^F(k_B T)$ from the scaling relation Eq. (51) and Eq. (52). $\langle \varepsilon \rangle$ represents the average relative error for the different $k_B T$ presented here.

defined depending on the characteristic length scale and the desired accuracy of the modeled system. Even though the numerical accuracy of the (stochastic) equation (9) has not been theoretically studied, for its deterministic counterpart (Eq (9) with $\mathbf{F}_i^b = 0$, which is an SPH discretization of the NS equation), the discretization error is (e.g., [45])

$$A \left(\frac{h}{L_c} \right)^2 + B \frac{n_{eq}^{-1/3}}{h} + C \frac{\chi}{h^p} \left(\frac{n_{eq}^{-1/3}}{h} \right)^\beta, \quad (53)$$

where A , B , and C are the scaling constant depending on the boundary and initial conditions, L_c is the characteristic length of the problem (i.e., the front perturbations wave-length), χ is the length scale characterizing the magnitude of perturbation of the particle arrangement from the Cartesian grid, p denotes the order of the differential operator, and β is an integer corresponding to the order of kernel used in the approximation. The considerations for choosing h in the SDPD method are the same as for choosing grid size in the grid-based methods. The particle density n_{eq} also defines the model resolution and should be chosen large enough as to maintain the second order of the discretization scheme. Our results shown in Fig 5 and Table I demonstrate that the numerical error in rPF-SDPD decreases with increasing n_{eq} , but remains within 5% for $n_{eq} = 27$, the smallest tested value of n_{eq} . Since the computational cost of the method scales as n_{eq}^2 (and one would want to chose n_{eq} as small as possible), $n_{eq} = 27$ would be a good choice to use in simulations. For the pairwise force given by Eq (17), the effect of the functional form of ϕ , as well as the value of parameters in ϕ given by Eq (20), was studied in [33] in the context of SPH. It was found that in the absence of thermal fluctuations, the choice of ϕ and the corresponding parameters (A , r_a , r_b , and k) affects the distribution of particles (and χ and the error in Eq (53)), and in this work we choose parameters that lead to a uniform distribution of particles and minimize χ and the discretization error. For the given choice of ϕ and the corresponding parameters, the only additional parameter that needs to be defined is $s_{\alpha\alpha}$. For a two-fluid system with interfacial surface tension σ , σ_0 can be found from Eq (52). Then, $s_{\alpha\alpha}$ is found from Eq (21).

Remark III.1 In the lattice model, we use the transition temperature T_c to construct a scaling relationship, but we do not simulate the regime of large thermal fluctuations near T_c . In practice, we note that for $-\frac{k_B T \Delta^3}{\epsilon} > 0.18$, SDPD particles of one fluid phase begin escaping into the fluid region of the other phase, i.e., the interface between the fluids diffuses, which is outside of the present study's scope. In this work, we consider mesoscale immiscible multicomponent flow, i.e., the flow with a fluctuating but clearly defined interface.

Remark III.2 The scaling expression (52) provides an accurate approximation of direct simulation results as demonstrated in Table I. However, it is not necessarily a unique expression. Other formulas in terms of $\frac{k_B T \Delta^3}{\epsilon}$ may be obtained.

Remark III.3 In the present study, we assume the interface has a radius of curvature much larger than h and can be locally approximated as flat. For an interface with a smaller radii of curvature, the surface tension may also depend on the local curvature. We will address this issue in the next section.

IV. NUMERICAL EXAMPLES

Here, we study the accuracy of the rPF-SDPD model. First, we show that rPF-SDPD yields consistent thermodynamic properties for bulk flow with thermal fluctuation. Next, we simulate a droplet of one fluid surrounded by another fluid and quantify the curvature dependence of the modeled surface tension. Finally, we study the dynamics of bubble coalescence and fluctuations of the fluid interface with and without gravity.

A. Thermodynamic properties

We first demonstrate that the present model accurately captures the thermodynamic properties of a bulk fluid, i.e., that in the presence of the pairwise forces \mathbf{F}_{ij}^{int} , the probability density function (PDF) of the x , y , and z velocity components are in good agreement with the Maxwell-Boltzmann distribution,

$$f_v(v_k) = \left(\frac{m}{2\pi k_B T} \right)^{\frac{3}{2}} \exp \left(-\frac{mv_k^2}{2k_B T} \right) \quad k = x, y, z, \quad (54)$$

and the local density fluctuations satisfy

$$\frac{\delta n(d)}{\langle n(d) \rangle} = \sqrt{\frac{k_B T}{\langle n(d) \rangle c^2 d^3}}, \quad (55)$$

where $\delta n(d)$ and $\langle n(d) \rangle$ are the standard deviation of density and average density within a cubic domain Ω_d with the edge size d , d^3 is the volume of Ω_d , and c is the speed of sound of the bulk fluid.

We simulate a single-component fluid in a three-dimensional $30 \times 30 \times 30h^3$ box in the absence of gravity. The simulations are initialized by placing particles on a Cartesian mesh with the grid size $\Delta = 0.25h$. The initial particle velocity is set to zero, and the fluid density is set to $n_{eq} = 64h^{-3}$. The pairwise forces are chosen to be the same as the numerical example presented in Section III A. At each time step, we compute the PDFs of the velocity components and local density $n(d)$ as

$$n(d) = \frac{\sum_i n_i \mathbf{I}_{i \in \Omega_d}}{\sum_i \mathbf{I}_{i \in \Omega_d}}, \quad (56)$$

where $\mathbf{I}_{i \in \Omega_d}$ is an indicator function equal to 1 if particle i is inside domain Ω_d and 0 otherwise; and n_i is found from Eq. (15).

Simulations with and without \mathbf{F}^{int} are performed. Figures 6(a) and 6(b) show that $f_v(v_k)$ ($k = x, y, z$) and $\delta n(d)/\langle n(d) \rangle$, obtained from the simulations with and without \mathbf{F}^{int} , agree well with the theoretical results given by Eqs. (54) and (55), respectively.

For $d = h$, $\delta n(d)/\langle n(d) \rangle$ is about 6% smaller than the theoretical prediction from Eq. (55). This difference arises because n_i in Eq. (56) is defined as a smoothed density with a smoothing length h . Therefore, for a small volume Ω_d with d comparable to h , the effective volume is a bit larger than d^3 , leading to an underestimation of density fluctuations. Nevertheless, a good agreement is achieved for $d > 1.6h$. These results demonstrate that rPF-SDPD yields consistent thermodynamic properties for the nearly incompressible fluids considered in this study.

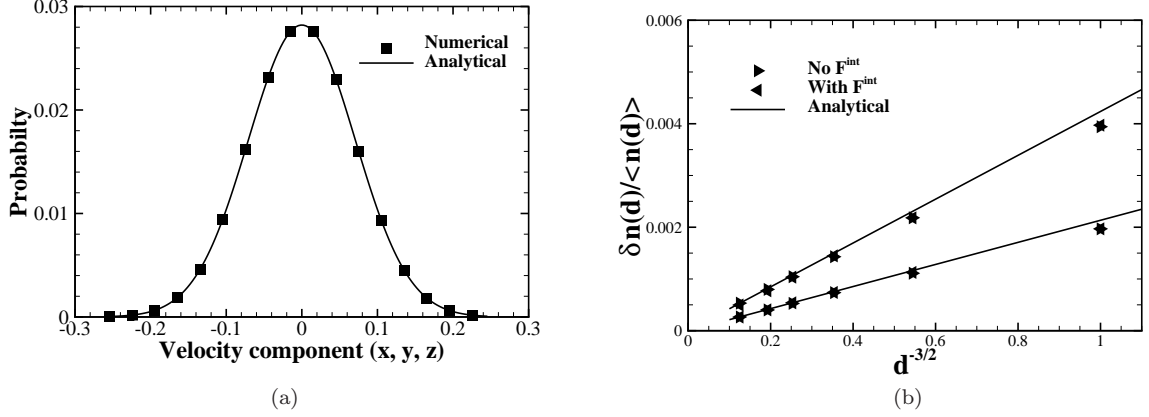


FIG. 6: Testing of the mesoscopic method: (a) Probability distribution of the velocity components of an individual mesoscopic particle with $k_B T = 0.005$. (b) Fluid density fluctuations within different volumes with $k_B T = 0.005$ and $k_B T = 0.02$.

B. Effect of interfacial curvature: surface tension of a droplet

In this section, we compute the surface tension of a three-dimensional droplet of fluid α immersed in fluid β . Previous studies show that on the molecular scale, surface tension depends on the curvature of the interface for the radius of curvature comparable with the molecular size (e.g., see Ref. [59].) Since the interaction forces in rPF-SDPD are similar to molecular forces, it is natural to expect the surface tension in rPF-SDPD to depend on the curvature for the radius of the curvature comparable with the particle size or h . In the following, we denote the surface tension of the droplet of radius R as $\tilde{\sigma}(R, k_B T)$ and explore the dependence of $\tilde{\sigma}$ on R for various temperatures $k_B T$ and number densities n_{eq} .

First, we simulate droplets with radii $2.5h$, $3.2h$ and $4.0h$, $k_B T = 0.001$, and $n_{eq} = 64.0h^{-3}$. The computational domain is $14 \times 14 \times 14h^3$ with the periodic boundary conditions in the x , y , and z directions. The droplet is initially placed in the center of the domain. Pairwise-force parameters are chosen so the surface tension corresponding to the flat interface approximation is $\sigma_0 = 2$. We compute the surface tension using two approaches, Eq. (23) and the Young-Laplace equation

$$\Delta P = \frac{2\tilde{\sigma}(R)}{R}, \quad (57)$$

where ΔP is the difference between the pressure inside and outside of the droplet. Figures 7(a) and 7(b) show ΔP and the stress components T_n and T_τ for the droplet radii greater than $2h$. For all three cases, the numerical values of $\tilde{\sigma}(R)$ agree well with the theoretical σ . These results show that for large radii R , $\tilde{\sigma}(R, k_B T)$ converges to the surface tension between two layers discussed in Section III, i.e., $\tilde{\sigma}(\infty, k_B T) = \sigma(k_B T)$.

Next, we compute the surface tension of the droplets with radii smaller than $4h$ for $n_{eq} = 27, 46.656$, and 64.0 at low temperature ($k_B T = 0.001$). Figure 7(c) depicts the simulation results. For all n_{eq} and $R < 2h$, $\sigma(R)$ decreases with decreasing R . This behavior is similar to that of the surface tension of nanoscale droplets, which can be approximated by [59]:

$$\tilde{\sigma}(R) = \sigma [1 - \exp(-R/R_0)], \quad (58)$$

where R_0 is a radius with the magnitude on the order of several fluid molecule diameters. In numerical models, including rPF-SDPD, $\tilde{\sigma}(R)$ is affected by the resolution when the radius of the curvature is of the same order as the spacial model resolution. In the present study, R_0 should be on the order of h or the size of an SDPD particle. In particular, $\tilde{\sigma}(R)$ converges more quickly to σ for larger spatial resolution n_{eq} , and, for all considered n_{eq} , $\tilde{\sigma}(R)$ approaches to σ for $R = 2.0h$.

We also examine the effect of thermal fluctuations on the curvature dependence of the surface tension. Figure 7(d) shows the size-dependent surface tension of a droplet $\tilde{\sigma}(R, k_B T)$ with $n_{eq} = 64$ and $k_B T = 0.001, 0.03$, and 0.05 for $\sigma(k_B T) = 2.0, 1.85$, and 1.43 . The parameters $s_{\alpha\beta}$ in the pairwise force are found from Eqs. (21) and (52). As $k_B T$ increases, $\tilde{\sigma}(R, k_B T)$ shows convergence to $\sigma(k_B T)$ at a slower rate than observed in Figure 7(c). This result is not unexpected, and can be understood qualitatively as follows: as $k_B T$ increases, the instantaneous interface

exhibits larger deviation from the equilibrium spherical interface due to larger thermal fluctuations, leading to more pronounced curvature dependence of the surface tension $\tilde{\sigma}(R, k_B T)$.

Finally, we perform additional simulations with various n_{eq} and observe that $\tilde{\sigma}(R, k_B T)$ converged to σ for the radii of curvature R satisfying

$$R \geq 2h + 10 \left(\frac{k_B T}{\sigma(k_B T)} \right)^{\frac{1}{2}}. \quad (59)$$

To simplify the notation, we use σ to represent $\tilde{\sigma}$ in the remaining part of the manuscript (if not otherwise specified).

Remark IV.1 We note that Eq. (59) is an empirical criterion to impose the prescribed surface tension $\sigma(k_B T)$ for interface with finite curvature. Theoretical analysis of thermal fluctuation effects on $\tilde{\sigma}(R, k_B T)$ is out of scope of the present study. The implications of Eq. (59) on numerics will be discussed in Section V.

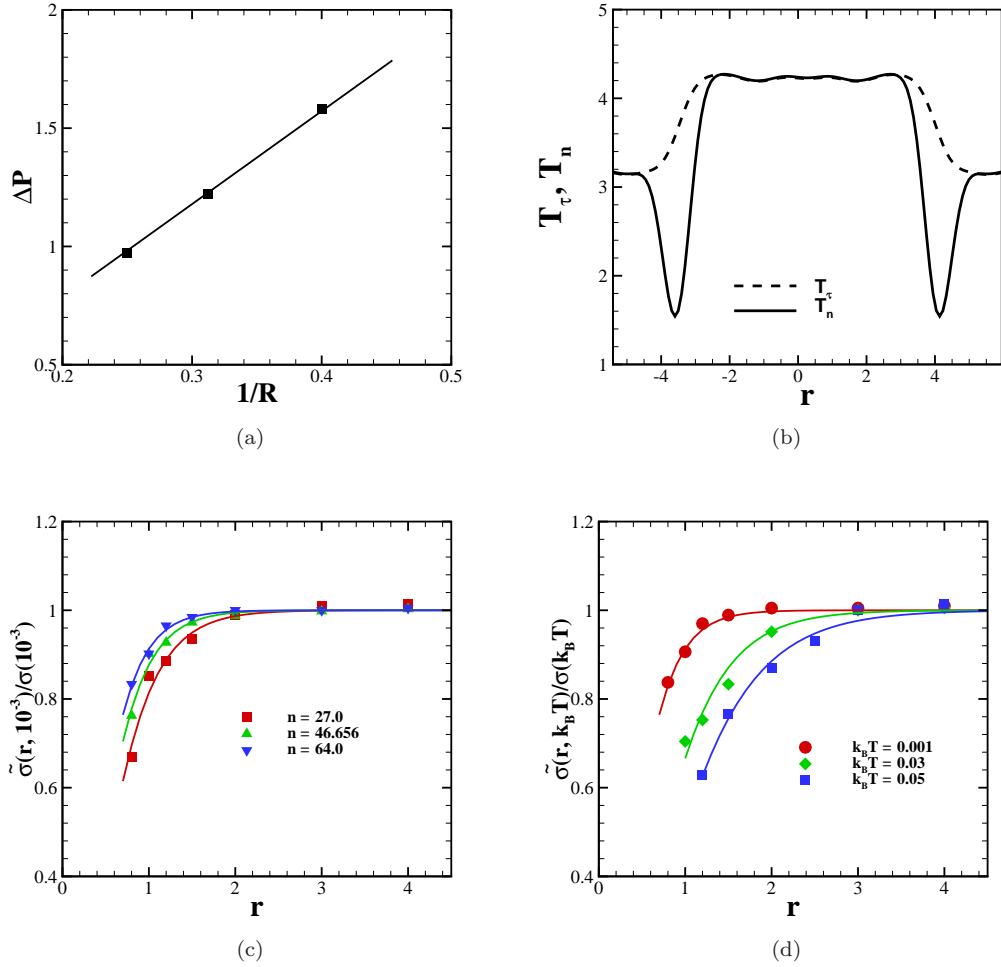


FIG. 7: (a) Pressure difference between the inside and outside domain of the droplet of radius $R = 2.5, 3.2$, and 4.0 with $n_{eq} = 64.0$ and $k_B T = 0.001$. The solid line represents the analytical prediction from the Young-Laplace relationship with $\tilde{\sigma}(R) = \sigma = 2.0$. (b) Normal and tangential hardy stress along the radial direction of the droplet of radius $R = 4.0$. (c) Surface tension $\tilde{\sigma}(R)$ computed from droplets of different radius R with $k_B T = 0.001$. The imposed flat interface surface tension $\sigma = 2.0$. (d) Surface tension $\tilde{\sigma}(R, k_B T)$ computed from droplets of different radius R and $k_B T$ with spatial resolution $n = 64.0$. The imposed flat interface surface tension is $\sigma(k_B T) = 2.0, 1.85$, and 1.43 , respectively.

C. Bubble coalescence

Next, we study the dynamic process of bubble coalescence in a two-phase fluid system similar to Ref. [60]. Two bubbles of radius $R = 4.0h$ are placed in a simulation domain $24 \times 12 \times 12h^3$ with the centers of the bubbles located at $[-4.25h, 0, 0]$ and $[4.25h, 0, 0]$. The periodic boundary condition is used in the simulations. The spatial resolution n_{eq} and speed of sound c are set to $64.0h^{-3}$ and 6.0 for both the bubbles (α fluid) and surrounding β fluid. The mass density ρ is 0.064 for α fluid and 64.0 for β fluid. The viscosity μ is 0.005 for α fluid and 0.5 for β fluid. As shown in Figure 8(a), we define the instantaneous neck radius R_{neck} of the bubble coalescence region by

$$R_{neck}(t) = \frac{1}{2\pi} \int_0^{2\pi} d\theta \int_0^\infty dr \delta \left(n^\alpha(\mathbf{r}, t) - \frac{n_{bulk}^\alpha}{2} \right), \quad \mathbf{r} = (0, r \cos \theta, r \sin \theta), \quad (60)$$

where $n^\alpha(\mathbf{r}, t)$ is the (time-dependent) smoothed number density of fluid α at point \mathbf{r} and n_{bulk}^α is the bulk number density of α fluid.

Under such conditions, the rate of bubble coalescence is controlled by the surface tension σ between α and β fluids [60]:

$$R_{neck}(t) = D_1 (\sigma R / \rho_{out})^{1/4} t^{1/2} = K t^{1/2}, \quad (61)$$

where D_1 is a dimensionless pre-factor, R is the radius of the bubble, and K is the growth rate. We simulate the coalescence process with the surface tension in the range $0.74 < \sigma < 3.88$. The radius of the largest curvature satisfies Eq. (59) in all of these cases.

Figure 8(b-c) shows the instantaneous neck radius R_{neck} for $k_B T = 0.003$. The growth rate K depends linearly on $\sigma^{1/4}$, which is consistent with Eq. (61). We also simulate the coalescence process with larger thermal fluctuations corresponding to $k_B T = 0.03$. In particular, we impose surface tension following two approaches: the low-temperature limit given by Eq. (21) and the thermal fluctuation scaling in Eq. (52). The resulting growth rates are shown in Fig. 8(d). For large surface tensions, both models yield consistent growth rates. However, when $-\frac{k_B T \Delta^3}{\epsilon}$ is large, Eq. (21) underestimates surface tension and results in slower growth rate. On the other hand, the scaling relation Eq. (52) yields a growth rate consistent with the theoretical result given by Eq. (61) for both $k_B T = 0.003$ and $k_B T = 0.03$.

D. Capillary waves

Finally, we examine the interfacial capillary waves in a two-component fluid system. The entire domain is $[-7, 7] \times [-7, 7] \times [-10, 10]h^3$ with fluid α placed between $-5h < z < 5h$ and fluid β occupying the rest of the domain. The initial particle density is set to $n_{eq} = 64h^{-3}$, and the speed of sound is set to $c = 6.0$. In the following, we present results at the interface located at $z = 5h$. The results for the interface at $z = -5h$ are identical. Because of thermal fluctuations, the interface between fluids α and β deviates from a flat plane with the instantaneous height $\eta(x, y)$ defined by

$$n^\alpha(x, y, \eta(x, y)) = \frac{n_{bulk}^\alpha}{2}, \quad (62)$$

where $n^\alpha(x, y, z)$ is the smoothed density of phase α at point (x, y, z) and n_{bulk}^α is the number density of α fluid in bulk.

For a fluid system in the absence of gravity, the capillary wave theory (CWT) [61, 62] predicts that the Fourier modes (a.k.a. the capillary wave spectra) $\hat{\eta}(\mathbf{q})$ of $\eta(x, y)$ are given by

$$\langle \hat{\eta}(\mathbf{q})^2 \rangle = \frac{k_B T}{\sigma |\mathbf{q}|^2 L^2}, \quad (63)$$

where $L \times L$ is the lateral interface domain. With the external gravity field g , acting along the z direction, there is an additional potential energy change due to the interface fluctuations, e.g., the work of exchanging the mass density of the lower fluid ρ_α to ρ_β . For each \mathbf{q} , the contribution to the potential energy difference ΔH_g is given by

$$\Delta H_g = \frac{1}{2} |\hat{\eta}(\mathbf{q})|^2 (\rho_\alpha - \rho_\beta) g L^2. \quad (64)$$

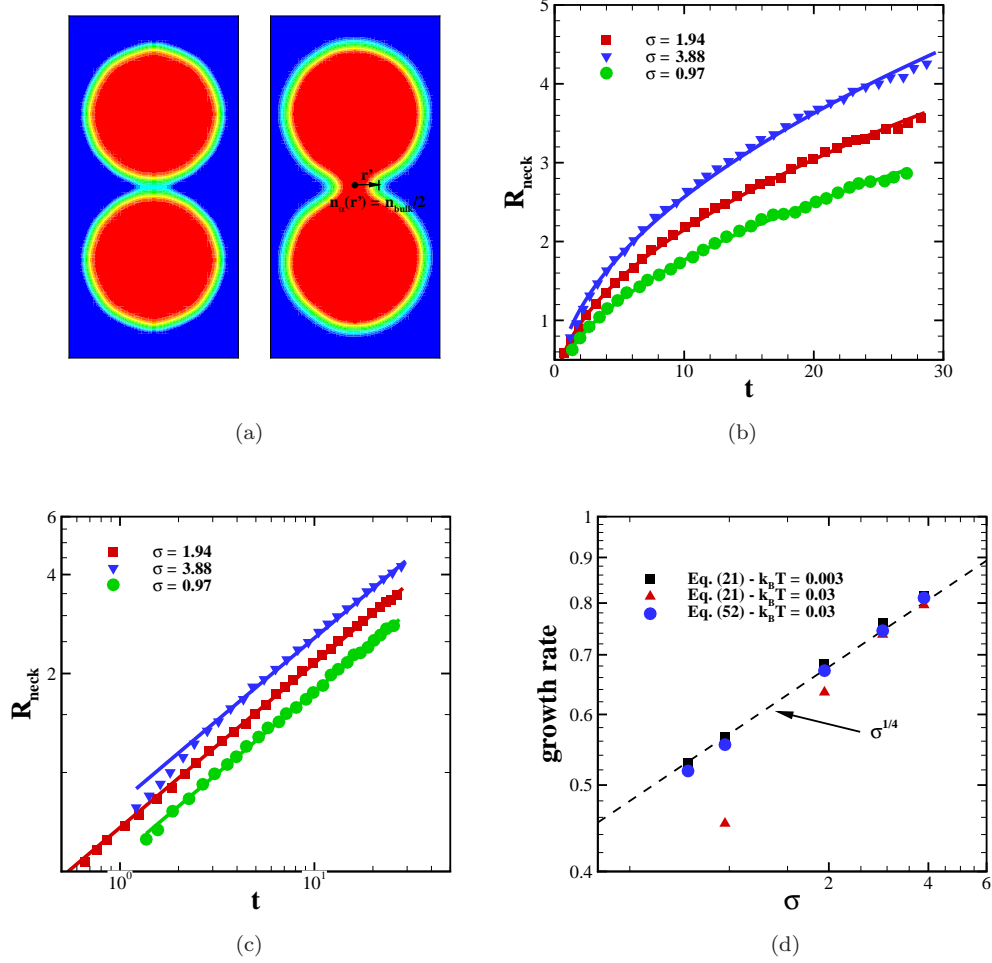


FIG. 8: (a) Sketch of the bubble coalescence procedure at initial (left) and intermediate (right) stage. For a specific radial direction θ , r' represents the radial distance from center such that $n_\alpha(r', \theta) = n_{bulk}/2$. (b) The instantaneous neck radius $R_{neck}(t)$ at $k_B T = 0.003$. (c) $R_{neck}(t)$ plotted in log-log scale. (d) The growth rate measured with different surface tensions and $k_B T = 0.003$ and $k_B T = 0.03$.

Therefore, the variance of $\hat{\eta}(\mathbf{q})$ of the fluctuating interface in the presence of gravity g is given by

$$\langle \hat{\eta}(\mathbf{q})^2 \rangle = \frac{k_B T}{\sigma |\mathbf{q}|^2 L^2 + (\rho_\alpha - \rho_\beta) g L^2} \quad (65)$$

First, we study the zero-gravity ($g = 0$) capillary wave spectra $\hat{\eta}(\mathbf{q})$ with $\rho_\alpha = \rho_\beta = 64.0$ and varying thermal fluctuations. The surface tension $\sigma = 2.0$ is imposed, following Eq. (52). Figures 9(a) and 9(b) show $\eta(x, y)$ with $k_B T = 0.004$, and 0.01 . As expected, $k_B T = 0.01$ yield larger interfacial fluctuations. Figure 9(c) shows the spectra $\hat{\eta}(\mathbf{q})$ at $k_B T = 0.004, 0.01, 0.03$, and 0.05 . For all $k_B T$, $\hat{\eta}(\mathbf{q})$ agrees well with Eq. (63) for low wave numbers and deviates from the CWT prediction for $|\mathbf{q}| \geq \frac{2\pi}{5h}$, where h is the support of the kernel W . This discrepancy is primarily due to the continuum assumption in CWT, where the interfacial energy is modeled as an increased surface area multiplied by the constant surface tension. However, for small length scales, local interfacial energy also depends on the local curvature and interactions between the SDPD particles (also shown in Section IV B). Therefore, the CWT prediction is not valid for high wave numbers (also see [46]). Remarkably, for $k_B T = 0.05$, we also present the spectrum obtained by imposing surface tension directly from Eq. (21); $|\hat{\eta}(\mathbf{q})|^2$ deviates from CWT prediction for all \mathbf{q} due to numerically overestimated interfacial surface tension at high temperatures.

Next, we examine the interfacial fluctuations with a non-zero gravity field and $k_B T = 0.01$. We consider two cases: (I) $\rho_\alpha = 64.0$, $\rho_\beta = 32.0$, and $g = 0.04$. (II) $\rho_\alpha = 32.0$, $\rho_\beta = 64.0$, and $g = 7.5 \times 10^{-3}$. Figures 10(a) and 10(b) show the instantaneous interface $g(x, y)$ for cases (I) and (II), respectively. For case (I), the lower fluid has larger

mass density than the upper fluid. Contributions from the change of gravity potential in Eq. (64) are positive, leading to dampened interfacial fluctuations in Figure 10(a) compared to Figure 9(b). In contrast, in case (II), the gravity contribution from Eq. (64) is negative, leading to increased interfacial fluctuations in Figure 10(b) compared to Figure 9(b).

Figure 10(c) shows $\hat{\eta}(\mathbf{q})$ for cases (I) and (II). Numerical results are in good agreement with the predictions from Eq. (65) for $|\mathbf{q}| \leq \frac{2\pi}{5h}$. At high wave numbers, $\hat{\eta}(\mathbf{q})$ deviates from Eq. (65) in a manner similar to the neutral case in Figure 9(c). For case (II), we choose g and σ , satisfying

$$\sigma q_0^2 > (\rho_\beta - \rho_\alpha)g, \quad (66)$$

where $q_0 = \frac{2\pi}{L}$ is the lowest wave number such that Rayleigh instability cannot be established. In contrast, if Eq. (66) is violated (e.g., $g = 0.014$ and $\sigma = 2.0$) Rayleigh instability will be develop as shown in Figure 10(d).

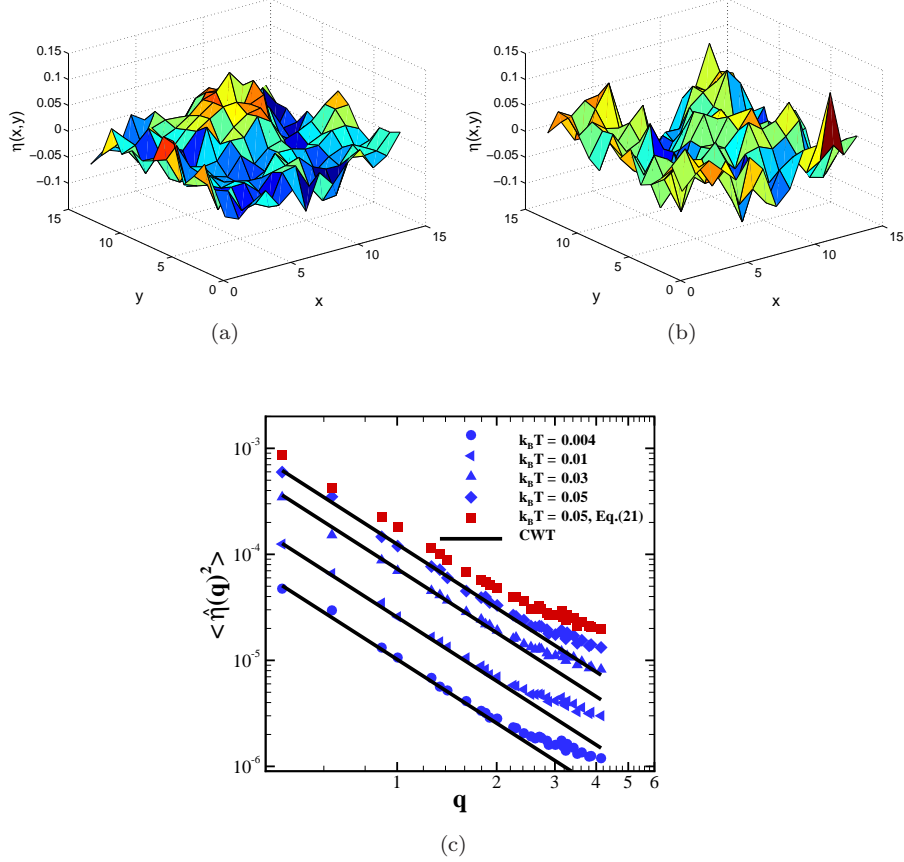


FIG. 9: (a) Instantaneous fluid height near the interface at $k_B T = 0.004$. (b) Instantaneous fluid height near the interface at $k_B T = 0.01$. (c) The capillary wave spectra measured at different temperatures. For $k_B T = 0.05$, spectrum with surface tension determined directly from Eq. (21) is also presented.

V. DISCUSSION

In this study, we proposed the rescaled Pairwise-Force Smoothed Dissipative Particle Dynamics (rPF-SDPD) method, a fully Lagrangian stochastic particle method designed to model mesoscopic multicomponent immiscible flow with thermal fluctuations. In the rPF-SDPD model, the surface tension between different fluid components is modeled via pairwise interaction forces added to the SDPD momentum conservation equation similar to the PF-SPH model [33]. In PF-SPH, a relationship between the surface tension and pairwise-force parameters (similar to Eq. (21)) is derived under a locally flat interface assumption. In this work, we demonstrated that, under moderate thermal fluctuations, the modeled surface tension deviates from the analytical result given by Eq. (21) and also depends on the model resolution. To accurately model fluids interfaces, we derived a universal scaling relationship between model

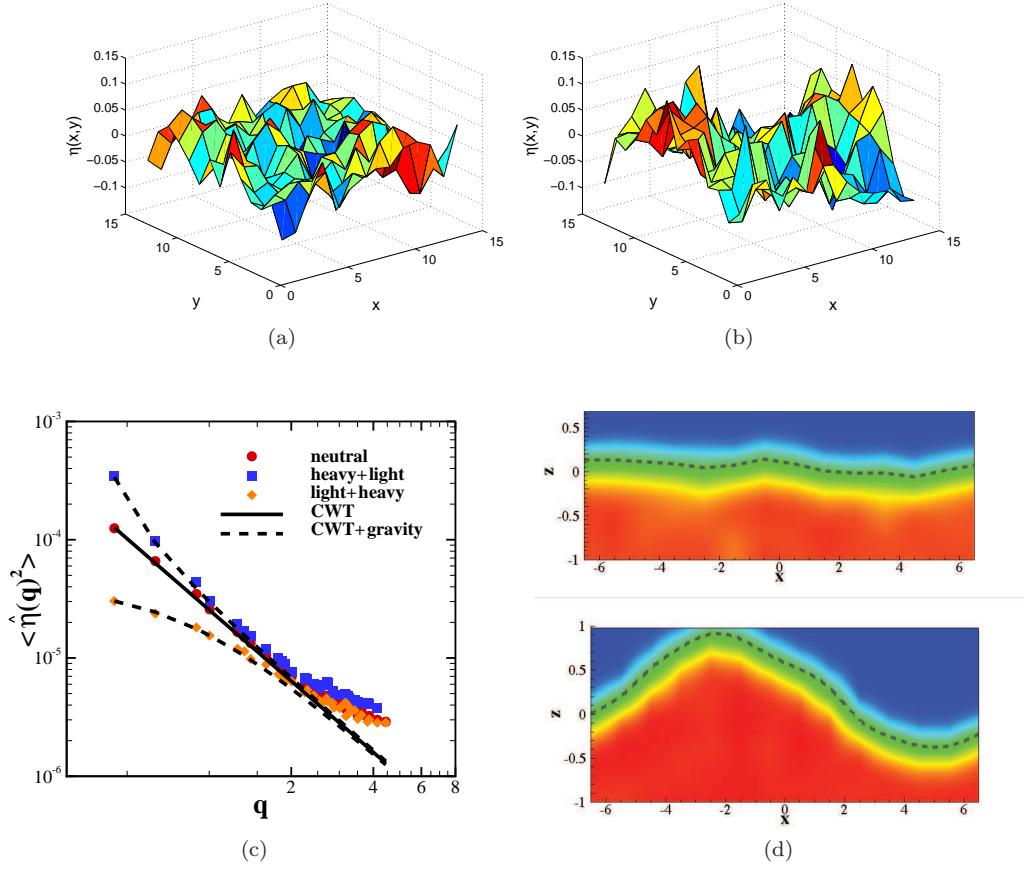


FIG. 10: (a) Instantaneous fluid height near the interface with $\rho_\alpha = 32.0$ and $\rho_\beta = 64.0$ at $k_B T = 0.01$. (b) Instantaneous fluid height near the interface with $\rho_\alpha = 64.0$ and $\rho_\beta = 32.0$ at $k_B T = 0.01$. (c) The capillary wave spectra measured at different gravity. (d) Instantaneous density field n_α near the fluctuation interface for $g = 0.0075$ (upper) and $g = 0.014$ (lower). For $g = 0.0075$, the two-phase fluid keeps stable fluctuation interface with spectrum shown in (c). For $g = 0.014$, Rayleigh instability is established and accompanied by giant fluctuation across the interface.

parameters (macroscopic surface tension in the absence of thermal fluctuations, temperature, model resolution, and pairwise interaction force) and the surface tension. To establish this relation, we constructed a coarse-grained Euler lattice model by mapping the SDPD particles on a discrete lattice based on a mean field theory. We demonstrated that the numerical results obtained from the present rPF-SDPD model agree well with the theoretical prediction based on the scaling relationship with deviation less than 5%.

Furthermore, we demonstrated that the rPF-SDPD model yields consistent thermodynamic properties of the bulk fluid under thermal fluctuations. Moreover, it accurately captures the dynamic processes, such as the bubble coalescence and the capillary wave spectrum under external gravity fields. These results suggest that the present method is well-suited for a wide application on multiphase immiscible flow on the mesoscopic scale where thermal fluctuations are pronounced, including nanoscale transport processes.

Finally, we observed that for interfaces with radii of curvature less than $2h$, the surface tension decreases with decreasing radii of curvature. Similar results are experimentally observed for real fluids, where the surface tension shows dependence on the radii of curvature for the radii on the order of the molecular size. We note that this length-scale-dependent surface tension (presented in Section IV B) raises some important issues that require future investigation. In most mesoscopic numerical methods (e.g., see Refs. [18, 29, 31]) for multiphase and multicomponent flows, the interfacial energy is imposed as the interface area multiplied by a prescribed surface tension coefficient. The implicit assumption therein is that the surface tension is a macroscopic property independent of local interface curvature, i.e., it remains constant as the spatial resolution of the interface increases. This assumption works well for most macroscopic (and many mesoscopic) multiphase flow systems. It also can be achieved for the present method by choosing proper scaling parameters so Eq. (59) is satisfied. However, additional consistency is required when we consider a multiphase flow system on the nanoscale. At this scale, arbitrarily increasing model resolution leads to

numerical divergence of interfacial fluctuations, i.e., $\sim \lim_{q_h \rightarrow \infty} \int_{q_l}^{q_h} \frac{1}{q^2} d^2 q = \infty$. On this length scale, surface tension also depends on the local curvature [63, 64] with behavior similar to Figure 7. For such systems, accurate fluctuation hydrodynamics modeling requires introduction of molecular fidelity in the form of an effective particle size and local compressibility, as discussed in Ref. [46]. Such use of additional collective variables will be explored in future work.

Acknowledgments

This research was supported by the U.S. Department of Energy, Office of Science, Office of Advanced Scientific Computing Research as part of the Collaboratory on Mathematics for Mesoscopic Modeling of Materials (CM4) and the New Dimension Reduction Methods and Scalable Algorithms for Nonlinear Phenomena project. CJM is supported by the DOE Office of Basic Energy Sciences, Division of Chemical Sciences, Geosciences and Biosciences. Pacific Northwest National Laboratory is operated by Battelle for the DOE under Contract DE-AC05-76RL01830. HL would like to thank Bin Zheng for helpful discussions.

References

-
- [1] J. M. Ortiz de Zárate, F. Peluso, and J. V. Sengers, The European physical journal. E, Soft matter **15**, 319 (2004), ISSN 1292-8941.
 - [2] B. Davidovitch, E. Moro, and H. Stone, Physical Review Letters **95**, 244505 (2005).
 - [3] M. Moseler and U. Landman, Science **289**, 1165 (2000).
 - [4] K. Kadau, C. Rosenblatt, J. L. Barber, T. C. Germann, Z. Huang, P. Carlès, and B. J. Alder, Proceedings of the National Academy of Sciences **104**, 7741 (2007).
 - [5] F. Quemeneur, J. K. Sigurdsson, M. Renner, P. J. Atzberger, P. Bassereau, and D. Lacoste, Proceedings of the National Academy of Sciences **111**, 5083 (2014).
 - [6] L. D. Landau and E. M. Lifshitz, *Fluid Mechanics* (Pregamon, New York, 1959).
 - [7] P. J. Atzberger, P. R. Kramer, and C. S. Peskin, Journal of Computational Physics **224**, 1255 (2007).
 - [8] P. J. Atzberger, Journal of Computational Physics **230**, 2821 (2011).
 - [9] N. K. Voulgarakis and J.-W. Chu, The Journal of Chemical Physics **130**, 134111 (2009).
 - [10] M. Serrano and P. Español, Phys. Rev. E **64**, 046115 (2001).
 - [11] J. B. Bell, A. L. Garcia, and S. A. Williams, Phys. Rev. E **76**, 016708 (2007).
 - [12] G. De Fabritiis, M. Serrano, R. Delgado-Buscalioni, and P. V. Coveney, Phys. Rev. E **75**, 026307 (2007).
 - [13] A. Donev, E. Vanden-Eijnden, A. L. Garcia, and J. B. Bell, Commun. Appl. Math. Comput. Sci. **5**, 149 (2010).
 - [14] A. Donev, J. B. Bell, A. de la Fuente, and A. L. Garcia, Phys. Rev. Lett. **106**, 204501 (2011).
 - [15] A. J. C. Ladd, Phys. Rev. Lett. **70**, 1339 (1993).
 - [16] P. Español and C. Thieulot, The Journal of Chemical Physics **118**, 9109 (2003).
 - [17] B. Z. Shang, N. K. Voulgarakis, and J.-W. Chu, The Journal of Chemical Physics **135**, 044111 (2011).
 - [18] A. Chaudhri, J. B. Bell, A. L. Garcia, and A. Donev, Physical Review E **90**, 033014 (2014).
 - [19] P. Hoogerbrugge and J. Koelman, Europhys. Lett. **19**, 155 (1992).
 - [20] P. Espanol and P. Warren, Europhysics Letters **30**, 191 (1995).
 - [21] R. D. Groot and P. B. Warren, Journal of Chemical Physics **107**, 4423 (1997).
 - [22] H. Lei, B. Caswell, and G. E. Karniadakis, Phys. Rev. E **81**, 026704 (2010).
 - [23] J. J. Monaghan, Annual Review of Astronomy and Astrophysics **30**, 543 (1992).
 - [24] J. J. Monaghan, Reports on Progress in Physics **68**, 1703 (2005).
 - [25] P. Español and M. Revenga, Phys. Rev. E **67**, 026705 (2003).
 - [26] M. Grmela and H. Öttinger, Physical Review E **56**, 6620 (1997).
 - [27] H. Öttinger and M. Grmela, Physical Review E **56**, 6633 (1997).
 - [28] J. Brackbill, D. Kothe, and C. Zemach, Journal of Computational Physics **100**, 335 (1992), ISSN 00219991.
 - [29] X. Y. Hu and N. A. Adams, Journal of Computational Physics **213**, 844 (2006).
 - [30] J. P. Morris, International Journal for Numerical Methods in Fluids **33**, 333 (2000).
 - [31] X. Hu and N. Adams, Journal of Computational Physics **228**, 2082 (2009).
 - [32] A. M. Tartakovsky and P. Meakin, Physical Review E **72**, 026301 (2005).
 - [33] A. M. Tartakovsky and A. Panchenko, Journal of Computational Physics **305**, 1119 (2016).
 - [34] X. Bian, S. Litvinov, R. Qian, M. Ellero, and N. A. Adams, Physics of Fluids **24** (2012).
 - [35] X. Bian and M. Ellero, Computer Physics Communications **185**, 53 (2014), ISSN 0010-4655.
 - [36] S. Litvinov, M. Ellero, X. Hu, and N. A. Adams, Phys. Rev. E **77**, 066703 (2008).
 - [37] A. Vázquez-Quesada, M. Ellero, and P. Español, The Journal of Chemical Physics **130**, 034901 (2009).
 - [38] X. Bian, M. Deng, Y.-H. Tang, and G. E. Karniadakis, Phys. Rev. E **93**, 033312 (2016).
 - [39] A. Vázquez-Quesada, M. Ellero, and P. Español, Phys. Rev. E **79**, 056707 (2009).
 - [40] W. Pan and A. M. Tartakovsky, Advances in Water Resources **58**, 41 (2013).
 - [41] Z. Xu, P. Meakin, A. M. Tartakovsky, and T. D. Scheibe, Physical Review E **83** (2011).
 - [42] E. Moeendarbary, T. Ng, and M. Zangeneh, International Journal of Applied Mechanics **1**, 737 (2009).
 - [43] C. Pastorino and A. G. Goicochea, *Selected Topics of Computational and Experimental Fluid Mechanics* (Springer International Publishing, Cham, 2015), chap. Dissipative Particle Dynamics: A Method to Simulate Soft Matter Systems in Equilibrium and Under Flow, pp. 51–79, ISBN 978-3-319-11487-3, URL http://dx.doi.org/10.1007/978-3-319-11487-3_3.
 - [44] J. Monaghan, Annual Review of Fluid Mechanics **44**, 323 (2012).
 - [45] A. Tartakovsky, N. Trask, K. Pan, B. Jones, W. Pan, and J. Williams, Computational Geosciences pp. 1–28 (2015).
 - [46] H. Lei, C. J. Mundy, G. K. Schenter, and N. K. Voulgarakis, The Journal of Chemical Physics **142**, 194504 (2015).
 - [47] L. D. Landau and E. M. Lifshitz, *Fluid Mechanics: Volume 6 (Course Of Theoretical Physics)* (Butterworth-Heinemann, 1987).
 - [48] J. P. Morris, Journal of Computational Physics **136**, 214 (1997), ISSN 00219991.
 - [49] A. M. Tartakovsky, P. Meakin, and A. L. Ward, Transport in Porous Media **76**, 11 (2009), ISSN 0169-3913.
 - [50] M. Guet-Kaplan, A. M. Tartakovsky, and B. Berkowitz, Water Resources Research **45**, 1 (2009), ISSN 0043-1397.
 - [51] A. M. Tartakovsky and P. Meakin, Vadose Zone Journal **4**, 848 (2005), ISSN 1539-1663.

- [52] J. Kordilla, A. M. Tartakovsky, and T. Geyer, *Advances in Water Resources* **59**, 1 (2013), ISSN 03091708.
- [53] J. J. S. Rowlinson and B. Widom, *Molecular theory of capillarity*, vol. 8 (Courier Dover Publications, 2002).
- [54] R. J. Hardy, *The Journal of Chemical Physics* **76**, 622 (1982).
- [55] M. Allen and D. Tildesley, *Computer Simulation of Liquids* (Clarendon Press, Oxford, 1989), ISBN 0198556454.
- [56] L. Rayleigh, *On the theory of surface forces. In Collected Papers*, vol. 3, Art. 176, pp. 397–425 (Dover, New York, 1964).
- [57] B. Widom, *The Journal of Physical Chemistry* **88**, 6508 (1984).
- [58] K. Dawson, *Physical Review A* **35**, 1766 (1987).
- [59] D. Kashchiev, *The Journal of chemical physics* **118**, 9081 (2003).
- [60] J. D. Paulsen, R. Carmigniani, A. Kannan, J. C. Burton, and S. R. Nagel, *Nature Communications* **5**, 3182 (2014).
- [61] F. P. Buff, R. A. Lovett, and F. H. Stillinger, *Phys. Rev. Lett.* **15**, 621 (1965).
- [62] R. Evans, *Advances in Physics* **28**, 143 (1979).
- [63] K. Lum, D. Chandler, and J. D. Weeks, *The Journal of Physical Chemistry B* **103**, 4570 (1999).
- [64] D. M. Huang, P. L. Geissler, and D. Chandler, *The Journal of Physical Chemistry B* **105**, 6704 (2001).